AIAA JOURNAL
Vol. 43, No. 8, August 2005

Head-On Collision of a Planar Shock Wave with Deformable Porous Foams

G. Malamud*
Ben-Gurion University of the Negev, 84105 Beer Sheva, Israel
D. Levi-Hevroni†
Nuclear Research Center—Negev, 84190 Beer Sheva, Israel
and
A. Levy‡
Ben-Gurion University of the Negev, 84105 Beer Sheva, Israel

Two-dimensional physical and numerical models for predicting the characteristics of the flowfield during an unsteady interaction between a planar shock wave moving through air and a deformable saturated porous material were developed using the representative-elementary-volume approach. The numerical model is based on a two-phase arbitrary Lagrangian Eulerian finite difference scheme to solve the flowfield governing equations. The multidimensional effects of the head-on collision were investigated. The physical model is validated by comparing the numerical predictions qualitatively and quantitatively to one- and two-dimensional shock-foam interaction experimental results. Good agreement was obtained both in one- and two-dimensional cases. It was found that wall friction results in shear bands (i.e., localized high vorticity), which affects the flowfield characteristics. Therefore, the common one-dimensional models are not valid in the vicinity of the shock tube sidewalls.

Nomenclature

C_α	=	specific heat capacities ratio for the α phase
c_α	=	shape factor for the α phase
$\boldsymbol{D}^{*H}$	=	dispersive heat tensor
e	=	specific internal energy
$\bar{e}^{\alpha}_{\alpha}$	=	average of intensive quality for the α phase
$\bar{F}$	=	isotropic macroscopic Forchheimer coefficient
G	=	shear modulus
g	=	specific gravity
$\boldsymbol{I}$	=	unit matrix
P	=	pressure
R	=	specific gas constant
S	=	interface between phases
T	=	temperature
$\boldsymbol{T}^{*}_{\alpha}$	=	tortuosity tensor of an α phase
t	=	time
$\bar{\boldsymbol{u}}$	=	velocity vector
V	=	volume
V_0	=	representative elementary volume (REV)
$\boldsymbol{x}_i$	=	unit vector in the ith direction
$\mathring{x}_i$	=	coordinate of a point in the REV relative to the REV center in the ith direction
$\boldsymbol{\alpha}$	=	unit vector normal to the solid–gas interface
$\alpha^{*\mathrm{II}}$	=	convection heat-transfer coefficient
γ	=	gas-phase specific heat capacities ratio
Δ_g	=	hydraulic radius of the gas-phase filled pores
$\varepsilon_{\mathrm{sk}}$	=	volumetric strain
$\boldsymbol{\varepsilon}_{\mathrm{sk}}$	=	strain tensor
$\bar{\eta}, \bar{\lambda}^{n,s}_{s}, \bar{\mu}^{n,s}_{s}$	=	Lame's constants for a thermoelastic solid matrix
$\bar{\lambda}^{''g}$	=	second kinematics viscosity of the gas phase
$\bar{\lambda}^{\alpha}_{\alpha}$	=	thermal conductivity for an α phase
$\bar{\mu}^{g}_{g}$	=	first kinematics viscosity of the gas phase
$\boldsymbol{\xi}$	=	unit vector perpendicular to the REV surface
ρ	=	density
$\boldsymbol{\sigma}_s$	=	stress of the solid phase
σ'_s	=	effective stress of the solid phase
ϕ_α	=	volumetric fraction of an α phase

Subscripts

g	=	gas
i, j, k	=	unit vectors in the orthogonal space coordinate system
s	=	solid
α	=	α phase

Received 6 June 2004; revision received 24 February 2005; accepted for publication 24 February 2005.

*Graduate Student, Pearlstone Center for Aeronautical Engineering Studies, Department of Mechanical Engineering.
†Researcher, P.O. Box 9046, Physics Department.
‡Professor, Pearlstone Center for Aeronautical Engineering Studies, Department of Mechanical Engineering; avi@bgu.ac.il.

I. Introduction

THE reflection phenomenon of shock waves over different geometries and the interaction phenomenon of shock or compression waves with porous media are two phenomena, which have gained much attention in the past two decades because of their application to many engineering fields. However, the full understanding of the physical phenomena occurring through the interaction has not been achieved. Many models were developed to reach such an understanding.[1–6] A comprehensive study regarding the flowfield governing equations was conducted in the Department of Mechanical Engineering in the Ben-Gurion University of the Negev, Beer Sheva, Israel. The leading approach of this study was a multiphase analysis based on a continuum approach of representative elementary volume (REV),[4,5,7–10] rather than a single-phase approach, for example, the mixing approach.[11–13]

In the multiphase approach, the porous medium is considered to be composed of few phases, namely, the solid matrix and the fluids that occupy its pores, which interact with each other. As a result, multiple flowfields (depending on the number of interacting phases) are developing inside the porous material, and description of the flowfield characteristics for each phase can be obtained. Baer[14] and Powers et al.[15] presented a one-dimensional two-phase analysis with air as the fluid phase. In their numerical solutions, they presented

a simplified analytical model for calculating the jump conditions across compaction waves in rigid porous materials.

Levy[9] and Levi-Hevroni[10] formulated the macroscopic mass, momentum, and energy balance equations for the fluid phase and the solid matrix, based on the REV approach.[7] These macroscopic balance equations were composed of averaged flux terms together with integrals of the microscopic exchange flux terms at the phase interfaces. Some unique macroscopic parameters, which emerged from the averaging process, were the tortuosity factor that represented a tensor associated with the solid matrix directional cosines, the hydraulic radius of the pores, and the porosity that represented the phases' volume fraction, filled by the fluids.

Bear and Sorek[16] developed the dominant forms of the macroscopic mass and momentum balance equations for a porous material under an isothermal abrupt pressure rise. In their study, it was shown that during the time period in which the dominant physical phenomena are considered to be inertial forces (i.e., nonlinear wave forms) the wave speed depends on the porous material structure.

Bear et al.[2] and Sorek et al.[8] extended the study of Bear and Sorek[16] and described the theoretical basis for the case of thermoelastic porous media. These studies were then followed by Levy et al.,[3] who introduced an additional Forchheimer term (an additional nonlinear macroscopic term, which was associated with the microscopic inertial term at the solid/fluid interface) and obtained a variety of nonlinear wave equation forms. Moreover, Levy et al.[3] presented the macroscopic mass, momentum, and energy balance equations for a saturated elastic rigid (i.e., assumed to have small deformations only) porous medium after an abrupt pressure and temperature jump, by conducting a dimensional analysis of these macroscopic balance equations.

Levy et al.[4] developed a one-dimensional two-phase numerical model that was based on a total-variation-diminishing (TVD) numerical scheme and solved numerically the set of the governing balance equations.[9] The numerical predictions were validated with experimental results,[17] and very good to excellent agreement was obtained.

Levi-Hevroni[10] and Levi-Hevroni et al.[18] presented a one-dimensional theoretical and numerical model for the case of shock impact on a deformable porous material (i.e., polyurethane foam). The hydrodynamic model was based on the assumption of large deformation rates for the porous material (unlike Levy et al.[5] and Levy,[9] who assumed a rigid porous media). As a result, Hooke's law was expressed, in terms of the stress rate as a function of the strain rate, rather than the stress as a function of the strain. This change resulted in an additional differential equation in the set of the governing equations, which, in turn, required an additional integration. The numerical predictions were compared with the experimental results of Skews et al.,[19] and good qualitative agreement was evident. The numerical simulation resulted in two different wave configurations (one for the solid phase and one for the gas phase) and therefore validated the two-phase model. The numerical simulation also suggested that the foam was compressed and decompressed for several cycles, in which the total stress direction is modified respectively.

Kitagawa et al.[20] studied experimentally and numerically the drag difference between steady and shocked gas flows passing through a porous body. Open-cell polyurethane foam was used for modeling the effective drag coefficients (Forchheimer and Darcy constants) in the macroscopic balance equations of Baer.[1] The numerical simulations were based on a first-order MUSCL-type TVD scheme and assumed small deformation for the solid phase. The comparison between the experimental data and the numerical prediction suggested that when the gas is shock induced the Forchheimer term is dominant and the Darcy term is negligible (as was presented in Levy[9] and Levy et al.[21]). It was also found from the experimental data that after the compression of the foam by the incident shock wave the foam equivalent stress is relaxed and its stress amplitude is equal to that of the gas pressure. This result contradicts the results obtained by Levi-Hevroni,[10] which suggests that the equivalent stress oscillates the front edge of the porous foam. A possible reason for this contradiction is the location of the pressure transducers in the shock tube, which can lead to a fault reading of the pressure caused by solid/fluid interface on the transducer surface.

Kitagawa et al.[22] had studied experimentally the head-on interaction of a shock wave with low-density polyurethane foam in a rectangle shock tube. A holographic interferometry visualization method and a high-speed video were used to determine the wave configuration and the foam surface location during the interaction. The experimental data suggest that a weak three-dimensional effect (from the shock-tube sidewall) exists as result of inertial and friction forces acting on the foam. This indicates the need for a two/three-dimensional numerical simulation capability, and that the one-dimensional models are valid only for predicting the flow characteristics at the shock-tube endwall and at the foam front surface.

An analytical model for solving the flowfield associated with regular reflections of oblique shock waves over rigid porous layers has been developed by Li et al.[23] The analytical model solved a set of 17 governing equations and could predict the properties of the fluid phase, along with the angles of the reflection and the diversion of the fluid velocity vectors from the shock waves and the porous surface. The predictions of the analytical model were validated by comparing them to the experimental data of Skews[24] and Kobayashi et al.[25]

Based on the REV concept, Malamud et al.[26] presented a two-dimensional theoretical and a numerical model for the shock-wave interaction with rigid porous material. Because a rigid porous wedge was assumed, a trivial solution for the solid balance equations was obtained. As a result, only the gas-phase flowfield was solved. The numerical predictions were validated with experimental results,[17,25,27] predictions of other one-dimensional numerical simulations,[5] and an analytical model.[23] Very good agreement was evident. The numerical model was based on a modified Lagrangian scheme, originally developed by Wilkins[28] for elastic plastic flow calculations. The modification of the numerical scheme converted it into an arbitrary Lagrangian Eulerian (ALE) scheme and implemented an Eulerian remesh technique.

In the present study, the two-dimensional two-phase model that is based upon the REV approach was solved numerically for the unsteady shock-wave interaction with deformable porous material. The hydrodynamic model considers large deformations and large deformation rates for the solid phase. The balance equations were solved in a Lagrangian approach for both the gas and solid phases. A remesh and interface tracking techniques were used in order to overcome the large grid deformation and to couple the solid and gas grids for the calculation of spatial coupling terms.

II. Theoretical Model

If we consider the porous medium to be a saturated continuum that is composed of interacting solid and fluid phases, then the macroscopic set of physical laws regarding the mass, momentum, and energy balances for the fluid phase and the solid matrix can be formulated by using the REV concept, presented by Bear and Bachmat.[7] A dimensional analysis of the macroscopic balance equations of Bear et al.[2] and Sorek et al.[8] was conducted by Levy,[9] who presented the governing macroscopic mass, momentum, and energy balance equations. The macroscopic balance equations were composed of averaged flux terms together with integrals of microscopic exchange flux terms at the solid/fluid interface. The averaging process produced new macroscopic terms related to the porous matrix spatial configuration.

A. Averaging Rules

The averaging technique of the various properties and balance equations was presented by Bear and Bachmat.[7] The volumetric fraction of the α phase ϕ_α inside the REV is defined by

$$\phi_\alpha = V_\alpha / V_0 \tag{1}$$

where V_α denotes volume of the α phase inside the REV and V_0 is the REV volume, which is defined (for a the two phase case) as $V_0 = \sum_\alpha V_\alpha$. The sum of the volumetric fractions of the phases inside the REV is equal to one ($\sum_\alpha \phi_\alpha = 1$).

The average of an intensive variable e_α of the α phase within the REV is given by

$$\bar{e}_\alpha^\alpha = \frac{1}{V_\alpha}\int_{V_\alpha} e_\alpha \, \mathrm{d}v \tag{2}$$

Averaging rules were defined for time and space derivatives, considering both the changes in the average quantity $\bar{e}_\alpha^\alpha$ and the relevant fluxes through the REV boundaries.

The average of a spatial derivative is given by

$$\overline{\frac{\partial e_\alpha^\alpha}{\partial x_i}}^\alpha = \frac{\partial \bar{e}_\alpha^\alpha}{\partial x_j}\boldsymbol{T}^*_{\alpha ij} + \frac{1}{\phi_\alpha V_0}\int_{S_{\alpha\beta}} \mathring{x}_i \frac{\partial e_\alpha}{\partial x_j}\xi_j \, \mathrm{d}s \tag{3}$$

where $\mathring{x}_i$ denotes the coordination of a point inside the REV relative to the REV center in the ith direction and $S_{\alpha\beta}$ represents the interface between the α phase and the β phase. The tortuosity tensor $\boldsymbol{T}^*_{\alpha ij}$ represents the microscopic configuration of the α-phase and the β-phase interface and therefore correlates with the tensor of directional cosines:

$$\boldsymbol{T}^*_{\alpha ij} = \frac{1}{\phi_\alpha V_0}\int_{S_{\alpha\alpha}} \mathring{x}_i \xi_j \, \mathrm{d}s \tag{4}$$

where $S_{\alpha\alpha}$ denotes the α-phase interface on the REV boundary.

The average of a time derivative is written by

$$\phi_g \overline{\frac{\partial e_g^g}{\partial t}}^g = \frac{\partial \phi_g \bar{e}_g^g}{\partial t} - \frac{1}{V}\int_{S_{\mathrm{gs}}} e_g \boldsymbol{u}\boldsymbol{\xi} \, \mathrm{d}s \tag{5}$$

where $\boldsymbol{u}$ is the gas-phase velocity and $\boldsymbol{\zeta}$ is a unit vector perpendicular to the surface and S_{gs} denotes the gas–solid interface.

B. Three-Dimensional Macroscopic Balance Equations

The macroscopic balance equations were obtained by applying the averaging process given in Levy et al.[5] on the microscopic balance equations for a compressible Newtonian fluid. The dispersive flux terms were considered to be negligibly small. The conservation balance equations for the gas and the solid phases are presented next.

1) Gas and solid mass balance equations, respectively:

$$\frac{\mathrm{D}}{\mathrm{D}t}\left(\phi_g \bar{\rho}_g^g\right) = -\phi \bar{\rho}_g^g \nabla \cdot \bar{\boldsymbol{u}}_g^g \tag{6}$$

$$\frac{\mathrm{D}}{\mathrm{D}t}\left(\phi_s \bar{\rho}_s^s\right) = -\phi_s \bar{\rho}_s^s \nabla \cdot \bar{\boldsymbol{u}}_s^s \tag{7}$$

where ρ_α, $\bar{\boldsymbol{u}}_\alpha$ are the density and velocity vector of the α phase, respectively.

2) Gas and porous medium momentum balance equations, respectively:

$$\begin{aligned}\phi_g \bar{\rho}_g^g \frac{\mathrm{D}}{\mathrm{D}t}\left(\bar{\boldsymbol{u}}_g^g\right) &= -\phi \boldsymbol{T}^*_g \nabla \bar{P}^g - \phi_g \bar{\rho}_g^g \boldsymbol{g}\boldsymbol{T}^*_g \nabla Z \\ &+ \bar{\mu}_g^g\left[\nabla^2\phi_g\left(\bar{\boldsymbol{u}}_g^g - \bar{\boldsymbol{u}}_s^s\right) + \nabla\cdot\left(\phi_g \nabla \bar{\boldsymbol{u}}_s^s\right)\right] \\ &+ \left(\bar{\mu}_g^g + \bar{\lambda}_g^{\prime\prime g}\right)\left\{\nabla\left[\nabla\phi_g\cdot\left(\bar{\boldsymbol{u}}_g^g - \bar{\boldsymbol{u}}_s^s\right)\right] + \nabla\left(\phi_g \nabla\cdot\bar{\boldsymbol{u}}_s^s\right)\right\} \\ &- \bar{\mu}_g^g c_f \phi_g \boldsymbol{\alpha}\cdot\frac{\bar{\boldsymbol{u}}_g^g - \bar{\boldsymbol{u}}_s^s}{\Delta_g^2} - \frac{c_f}{2\Delta_g^2}\boldsymbol{F}\phi_g\bar{\rho}_g^g\left(\bar{\boldsymbol{u}}_g^g - \bar{\boldsymbol{u}}_s^s\right)\left(\bar{\boldsymbol{u}}_g^g - \bar{\boldsymbol{u}}_s^s\right)\end{aligned} \tag{8}$$

$$\begin{aligned}\phi_g \bar{\rho}_g^g \frac{\mathrm{D}}{\mathrm{D}t}\left(\bar{\boldsymbol{u}}_g^g\right) + \left(\phi_s \bar{\rho}_s^g\right)\frac{\mathrm{D}}{\mathrm{D}t}\left(\bar{\boldsymbol{u}}_s^s\right) &= -\left(\phi_g \bar{\rho}_g^g + \phi_s \bar{\rho}_s^s\right) g \nabla Z \\ &+ \frac{\bar{\mu}_g^g}{\phi_g}\left[\nabla^2\phi_g\left(\bar{\boldsymbol{u}}_g^g - \bar{\boldsymbol{u}}_s^s\right) + \nabla\nabla\cdot\phi_g\left(\bar{\boldsymbol{u}}_g^g - \bar{\boldsymbol{u}}_s^s\right)\right] \\ &+ \frac{\bar{\lambda}_g^{\prime\prime g}}{\phi_g}\nabla\nabla\cdot\phi_g\cdot\left(\bar{\boldsymbol{u}}_g^g - \bar{\boldsymbol{u}}_s^s\right) + \bar{\mu}_g^g\left(\nabla^2\bar{\boldsymbol{u}}_s^s + \nabla\nabla\cdot\bar{\boldsymbol{u}}_s^s\right) \\ &+ \bar{\lambda}_g^{\prime\prime g}\nabla\nabla\cdot\bar{\boldsymbol{u}}_s^s + \nabla\boldsymbol{\sigma}'_s - \nabla\bar{P}^g\end{aligned} \tag{9}$$

where $\boldsymbol{\sigma}'_s$ denotes the effective solid stress tensor, which includes the gaseous-phase effect, defined by Terzaghi[29] as

$$\boldsymbol{\sigma}'_s = (1-\phi_g)(\boldsymbol{\sigma}_s - P\boldsymbol{I}) \tag{10}$$

3) Gas and solid energy balance equations, respectively:

$$\begin{aligned}\frac{\mathrm{D}}{\mathrm{D}t}\left\{\phi_g\bar{\rho}_g^g\left[C_g\bar{T}_g^g + \frac{\left(\bar{\boldsymbol{u}}_g^g\right)^2}{2}\right]\right\} &= \left\{\phi_g\bar{\rho}_g^g\left[C_g\bar{T}_g^g + \frac{\left(\bar{\boldsymbol{u}}_g^g\right)^2}{2}\right]\right\}\nabla\cdot\bar{\boldsymbol{u}}_g^g \\ &- \alpha^{*\mathrm{II}}\left(\bar{T}_g^g - \bar{T}_s^s\right) + \boldsymbol{T}^*_g\bar{P}^g\bar{\boldsymbol{u}}_s^s\nabla\phi_g - \boldsymbol{T}^*_g\nabla\left(\phi_g\bar{P}^g\bar{\boldsymbol{u}}_g^g\right) \\ &+ \nabla\cdot\left[\phi_g\boldsymbol{D}^{*\mathrm{II}}\nabla\left(C_g\bar{\rho}_g^g\bar{T}_g^g\right) + \phi_g\bar{\lambda}_g^g\nabla\bar{T}_g^g\right] \\ &- \left[\bar{\mu}_g^g c_f\phi_g\boldsymbol{\alpha}\cdot\frac{\bar{\boldsymbol{u}}_g^g - \bar{\boldsymbol{u}}_s^s}{\Delta_g^2} + \frac{c_f}{2\Delta_g^2}\boldsymbol{F}\phi_g\bar{\rho}_g^g\left(\bar{\boldsymbol{u}}_g^g - \bar{\boldsymbol{u}}_s^s\right)\left(\bar{\boldsymbol{u}}_g^g - \bar{\boldsymbol{u}}_s^s\right)\right]\bar{\boldsymbol{u}}_s^s\end{aligned} \tag{11}$$

$$\begin{aligned}\frac{\mathrm{D}}{\mathrm{D}t}\left\{\phi_s\bar{\rho}_s^s\left[C_s\bar{T}_s^s + \frac{\left(\bar{\boldsymbol{u}}_s^s\right)^2}{2}\right]\right\} &= \left\{\phi_s\bar{\rho}_s^s\left[C_s\bar{T}_s^s + \frac{\left(\bar{\boldsymbol{u}}_s^s\right)^2}{2}\right]\right\}\nabla\cdot\bar{\boldsymbol{u}}_s^s \\ &+ \alpha^{*\mathrm{II}}\left(\bar{T}_g^g - \bar{T}_s^s\right) + \boldsymbol{T}^*_g\bar{P}^g\bar{\boldsymbol{u}}_s^s\nabla\cdot\left(\phi_s\bar{P}^g\bar{\boldsymbol{u}}_s^s\right) - \boldsymbol{T}^*_g\bar{P}^g\bar{\boldsymbol{u}}_s^s\nabla\phi_g \\ &- \nabla\cdot\left(\sigma'_s\bar{\boldsymbol{u}}_s^s\right) - \nabla\cdot\left[\phi_s\bar{\lambda}_s^s\nabla\bar{T}_s^s\right] + \left[\bar{\mu}_g^g C_f\phi_g\boldsymbol{\alpha}\cdot\frac{\bar{\boldsymbol{u}}_g^g - \bar{\boldsymbol{u}}_s^s}{\Delta_g^2}\right. \\ &\left. + \frac{c_f}{2\Delta_g^2}\boldsymbol{F}\phi_g\bar{\rho}_g^g\left(\bar{\boldsymbol{u}}_g^g - \bar{\boldsymbol{u}}_s^s\right)\left(\bar{\boldsymbol{u}}_g^g - \bar{\boldsymbol{u}}_s^s\right)\right]\bar{\boldsymbol{u}}_s^s\end{aligned} \tag{12}$$

Hereafter we will refer to the macroscopic properties, and hence we will omit the average sign of any quantity (i.e., $\bar{e}^\alpha$).

C. Assumptions

The three-dimensional macroscopic balance equations were rewritten for the case of dominant nonlinear terms, as in the case of shock-wave interaction with a deformable porous medium. The assumptions used for the model were made on the basis of the dimensional analysis of Levy[9] and the parametric research of Levy et al.[30] and are listed next.

The model assumptions are as follows:

1) The gas is ideal and perfect (i.e., inviscid, thermally nonconductive and obeys to a perfect gas equation of state).

2) The dispersive and the diffusive mass fluxes of the gaseous phase, and the dispersive flux of the solid phase, are much smaller than the corresponding advective fluxes and can, therefore, be neglected.

3) The dispersive momentum fluxes of the gaseous and the solid phases are much smaller than their advective fluxes and can, therefore, be neglected.

4) The conductive and the dispersive heat fluxes of the gaseous phase are negligibly small when compared to their advective heat fluxes.

5) The microscopic solid/fluid interfaces are material surfaces with respect to the mass of both the gaseous and the solid phases.

6) The solid matrix is flexible and is assumed to be elastic perfectly plastic.

7) The stress–strain relationships for the solid matrix, at the microscopic level, and for the solid matrix, at the macroscopic level, have the same form.

8) The material of which the skeleton of the porous material is made is incompressible.

9) The specific heat capacity at constant volume of the fluid C_f is constant.

10) There are no external energy sources.

11) The energy associated with viscous dissipation is negligibly small.

12) The rate of the heat transferred between the gaseous and solid phases is negligibly small. Therefore, energy changes in the solid are negligibly small.

13) The solid phase is isothermal.
14) The last assumption is two-dimensional flow.

D. Two-Dimensional Governing Equations

Based on the assumptions just mentioned and in order to implement a Lagrangian numerical scheme, the macroscopic balance equations were rewritten in the following nonconservative form.

Mass balance equations for the gaseous and solid phases, respectively:

$$\frac{\mathrm{D}(\phi\rho_g)}{\mathrm{D}t} = -\phi\rho_g\nabla\boldsymbol{u}_g \tag{13}$$

$$\frac{\mathrm{D}[(1-\phi)\rho_s]}{\mathrm{D}t} = -[(1-\phi)\rho_s]\nabla\boldsymbol{u}_s \tag{14}$$

Momentum balance equations for the gaseous and solid phases, respectively:

$$\frac{\mathrm{D}}{\mathrm{D}t}(\phi\rho_g\boldsymbol{u}_g) = -\phi\rho_g\boldsymbol{u}_g\nabla\boldsymbol{u}_g - \phi\boldsymbol{T}_g^*\nabla P_g - \tilde{\boldsymbol{F}}_{\mathrm{gs}}\phi\rho_g|\boldsymbol{u}_{\mathrm{gs}}|\boldsymbol{u}_{\mathrm{gs}} \tag{15}$$

$$\frac{\mathrm{D}}{\mathrm{D}t}[(1-\phi)\rho_s\boldsymbol{u}_s] = -(1-\phi)\rho_s\boldsymbol{u}_s\nabla\boldsymbol{u}_s + \nabla\boldsymbol{\sigma}_s - \left(\boldsymbol{I} - \phi\boldsymbol{T}_g^*\right)\nabla P_g + \tilde{\boldsymbol{F}}_{\mathrm{gs}}\phi\rho_g|\boldsymbol{u}_{\mathrm{gs}}|\boldsymbol{u}_{\mathrm{gs}} \tag{16}$$

Energy balance equation for the gaseous phase:

$$\frac{\mathrm{D}}{\mathrm{D}t}\left[\phi\rho\left(e + \boldsymbol{u}\frac{\boldsymbol{u}}{2}\right)\right]_g = -\left[\phi\rho u\left(e + \boldsymbol{u}\frac{\boldsymbol{u}}{2}\right)\right]\nabla\cdot\boldsymbol{u} - \phi\boldsymbol{T}_g^*\boldsymbol{u}_g\nabla P_g - \tilde{\boldsymbol{F}}_{\mathrm{gs}}\phi\rho_g\boldsymbol{u}_{\mathrm{gs}}\boldsymbol{u}_{\mathrm{gs}}\boldsymbol{u}_s \tag{17}$$

Because it was assumed that the solid phase is isothermal, the solid-phase energy equation was not solved.

E. Constitutive Model

The hydrodynamic model for the solid phase assumes an elastic perfectly plastic material. This assumption and the common high strain rate that is developed in a deformable porous material under dynamic load dictates a rate depended strain-stress model. The macroscopic strain rate tensor for the solid matrix is defined as

$$\dot{\varepsilon}_{ij_s} = \frac{1}{2}\left(\frac{\partial u_i}{\partial x_j} + \frac{\partial u_j}{\partial x_i}\right)_s \tag{18}$$

where u_i denotes the velocity in the ith direction. The solid-phase stress tensor was defined by

$$\boldsymbol{\sigma}_{ij_s} = -P_s\delta_{ij} + \boldsymbol{\tau}_{ij_s} \tag{19}$$

The solid matrix macroscopic pressure is defined as

$$P_s \equiv -\tfrac{1}{3}\boldsymbol{\sigma}_{kk} = -\tfrac{1}{3}(\boldsymbol{\sigma}_{11} + \boldsymbol{\sigma}_{22} + \boldsymbol{\sigma}_{33}) \tag{20}$$

The Hooke's law with respect to time, together with Eqs. (18) and (19), is written as

$$\dot{\boldsymbol{\tau}}_{ij_s} = 2G\left(\dot{\boldsymbol{\varepsilon}}_{ij} - \tfrac{1}{3}\dot{\boldsymbol{\varepsilon}}_{kk}\delta_{ij}\right) \tag{21}$$

The solid-phase stress tensor $\dot{\boldsymbol{\sigma}}_{ij_s}$, as appears in Eq. (19), can be derived by simply integrating $\dot{\boldsymbol{\tau}}_{ij_s}$ with respect to time:

$$\boldsymbol{\tau}_{ij_s} = \int \dot{\boldsymbol{\tau}}\,\mathrm{d}t \tag{22}$$

The von Mises yield criteria are written as

$$\boldsymbol{\tau}_1^2 + \boldsymbol{\tau}_2^2 + \boldsymbol{\tau}_3^2 \le \tfrac{2}{3}(Y^0)^2 \tag{23}$$

where Y^0 denotes the yield stress. Because an elastic perfectly plastic material was assumed, if the inequality (23) does not sustain, the solid stress tensor is multiplied by the factor $\sqrt{(2/3)Y^0}/\sqrt{(\boldsymbol{\tau}_1^2 + \boldsymbol{\tau}_2^2 + \boldsymbol{\tau}_3^2)}$. The hydrostatic stress is independent of plastic deformation and therefore could be calculated from the equation of state. Recall that it was assumed that the energy change of the solid phase is negligibly small; therefore, the equation of state for the solid phase can be written in the form[31]

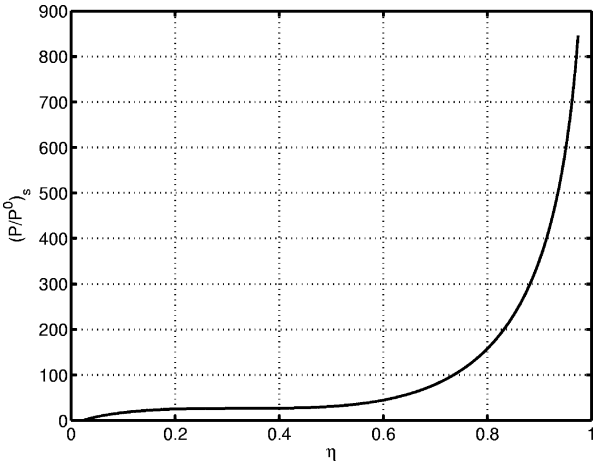

Fig. 1 Normalized pressure as a function of solid porosity as was described by Eq. (24).

$$P = \bar{E}_s\eta_{\max}\left[-\ell_n(1-\eta/\eta_{\max}) - B(\eta/\eta_{\max})^n\right] \tag{24}$$

In this equation, $\bar{E}_s$ denotes the macroscopic elastic modulus, η denotes the volumetric strain that was defined as $\eta = 1 - \bar{\rho}_s^0/\bar{\rho}_s$, and $\eta_{\max}$ denotes the maximal volumetric strain. Because the porous material is assumed to be microscopically incompressible, $\eta_{\max}$ is simply defined by $\eta_{\max} = \phi$ deg. The material properties n and B are determined as 1.445 and 1.689, respectively, according to experimental results presented by Zaretsky and Ben-Dor.[31] Kitagawa et al.[22] found a characteristic hysteresis cycle during the foam stress loading and unloading. This hystresis phenomenon was neglected in the present work. The normalized pressure P/P^0 that was used by the simulation as a function of solid porosity is presented in Fig. 1. The Yield stress Y^0 and the shear modulus G are given by[32]

$$G = \tfrac{3}{8}E_s(1-\phi_s)^2, \qquad Y^0 = 0.05E_s(1-\phi_s)^2 \tag{25}$$

The equation of state for the gaseous phase is taken to be the perfect-gas equation:

$$P_g = \rho_g RT_g = (\gamma - 1)\rho_g e_g \tag{26}$$

F. Wall Effects

The planar interaction of a shock wave moving in a finite space (i.e., shock tube) can be affected by two- and three-dimensional effects (i.e., wall-friction effects). In most cases the influence of the walls on the shock wave, which propagates in the gas phase, is negligible in comparison to that on the solid phase. Although the physics of the foam/wall interaction is quite complicated, a simple model that describes the friction force as function of the foam stress on the wall was assumed for a qualitative description of the phenomena. The simple effective Coulomb friction model was used to account for the effect of the wall friction on the porous sample. The model assumes that the wall-friction force F_D is proportional to the normal force acting on the surface N, that is, $F_D \propto N$. The normal force N is proportional to the foam stress tensor components normal to the wall surface, that is, $N \propto P_s - S_{1s}$, where S_{1s} is the deviator component. Therefore, the friction force per unit area A is expressed as

$$F_D/A = \mu_s(P_s - S_{1s}) \tag{27}$$

The friction coefficient μ_s usually depends on the wall/foam material. A representative value of 0.01 was considered for all of the

calculations that will be presented in this study. The wall-friction model was implemented in the numerical code, and its influence on the predictions of the numerical simulations was validated with the experimental results that were published by Kitagawa et al.[22] As will be shown, good qualitative agreement was evident.

III. Numerical Model

In the present work, a Lagrange numerical scheme, originally developed by Wilkins[28] for elastic-plastic flow, was modified and extended to solve the two-dimensional two-phase interaction of a shock wave with a deformable porous material. The modified numerical scheme is composed of an ALE scheme with an Eulerian remesh technique and an interface-tracking scheme.

The prediction of the flowfield characteristics for each time step is achieved by a Lagrangian solution of the balance equations (12–17). Because the gas and the solid phases are capable of moving independently in space, the numerical grid was remeshed to the original grid, and the transferred terms between the phases were calculated. Another advantage of remesh technique is to avoid the large numerical strains during each time step because of the nonsymmetric movement of the grid vertices. An interface-tracking scheme was used to determine the exact position of the solid-phase interface during the calculation. A detailed description of the numerical model can be found in Malamud et al.[26]

All of the numerical simulations that were conducted and presented in this work were fully two dimensional, with square numerical cells of 1 by 1 mm. A symmetry boundary condition over the $y = 0$ line and a free-slip boundary condition over all shock tube walls were assumed. For the results presented in Sec. IV.B, the wall-friction model (presented in Sec. II.F) was implemented at the wall boundary of the solid phase.

IV. Comparisons Between the Numerical Predictions and Experimental Data

To validate the physical and the numerical models, it was decided to compare the prediction of the numerical simulations with available experimental data. In the following section, the validation of the numerical simulations predictions for one- and two-dimensional cases will be presented.

A. Comparisons with One-Dimensional Experimental Results

Figure 2 presents a comparison between the predictions of the numerical simulation with experimental results of Skews et al.[19] for the pressure histories on the shock-tube endwall as obtained when a planar shock interacts with polyurethane foam. The polyurethane Young modulus E_s and Poisson ratio ν were presented by Gibson and Ashby[31] and were determined as 45 MPa and $\frac{1}{3}$, respectively. The initial conditions for the experiment and simulation are presented in the first line of Table 1.

The pressure that operates on the shock-tube endwall is a composition of both the gas-phase and the solid-phase transmitted waves as arrived and interact with the shock tube end wall. Its amplitude depends on the relative interaction area between the wall and the phases. In this study, it was assumed that the equivalent pressure that operates on the shock-tube endwall can be estimated by $P_{\text{eq}} = \phi P_g + (1-\phi) P_s$. As can be seen in Fig. 2, the numerical prediction of the shock-wave endwall pressure is in good agreement with the experimental data of Skews et al.,[19] both with the wave amplitude and its qualitative shape.

B. Comparison with Three-Dimensional Experimental Results

Kitagawa et al.[22] conducted experiments in a rectangular shock tube for the head-on interaction of a planer shock wave with polyurethane foam. Holographic interferometery of the polyurethane foam during the interaction with the shock wave was presented (Fig. 3). Based on Fig. 3, Kitagawa et al.[22] demonstrate the wall effect and claim that one-dimensional models are not reliable and therefore should not be considered. As can clearly be seen, the foam is distorted in a typical λ shape form (marked as area 1 in Fig. 3), which is coupled to the stress wave moving in the foam. Another area of low density is also clearly shown (marked as area 2 in Fig. 3), closer to the foam front. This typical structure can be related to the high strained area near the shock-tube sidewall, resulted from the foam wall friction and distorted the wave configuration. To simulate this interaction, the initial conditions for the simulation were taken from Kitagawa et al.[22]; however, because the geometrical and physical constants of the foam were not published it was decided to use the same constants as used to predict the one-dimensional case described in Sec. IV.A. The initial conditions and geometrical constants used in the simulation are presented in the second line of Table 1.

A comparison between the x–t diagram for the center of the foam front as was extracted from the experimental results presented by Kitagawa et al.,[22] and the numerical simulation is presented in Fig. 4. Good agreement is evident. This indicates that the theoretical model can predict the gas/foam interaction correctly. As can be seen, the foam front moves with approximately constant velocity.

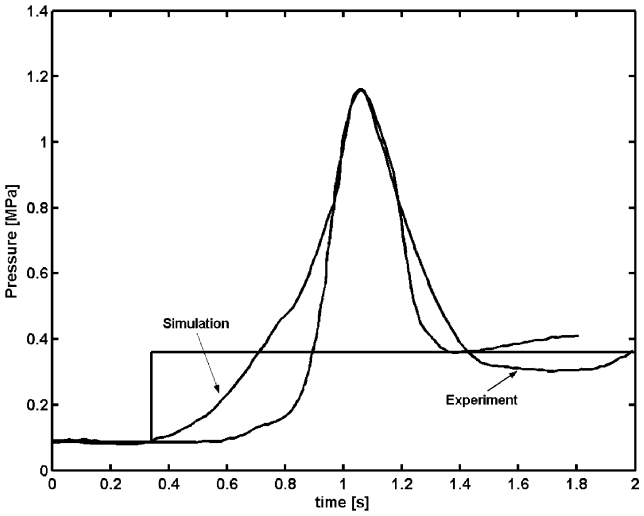

Fig. 2 Comparison between the predictions of the numerical simulation and the experimental results of Skews et al.[19] for the pressure histories on the shock-tube endwall as were obtained for the head-on interaction of shock wave with polyurethane foam.

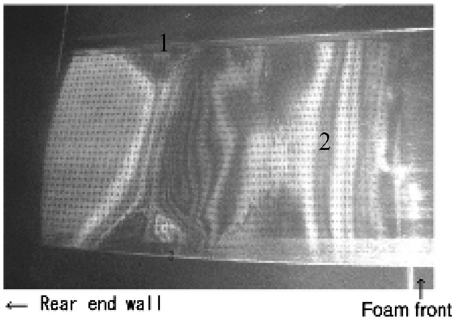

Fig. 3 Holographic interferometery of a polyurethane foam during and unsteady interaction with a shock wave.[22]

Table 1 Initial conditions for the experiments of Skews et al.[19] and Kitagawa et al.[22] and the corresponding numerical simulations

Figure	M_i	T_0, K	P_0, kPa	Foam length, mm	$\tilde{F}$	Porosity ϕ^0	$\tilde{\rho}_s^0$, kg/m^3	T^*
2	1.4	290	83.0	70	1100	0.98	26	0.6
3, 4, 6, 7	1.25	300	100.0	1200	700	0.974	28	0.5

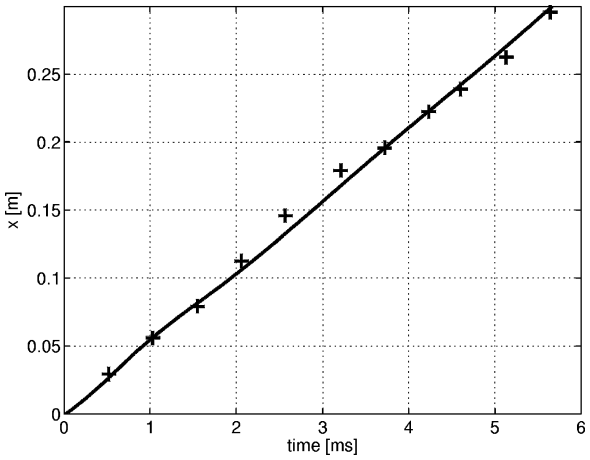

Fig. 4 Comparison for the center of foam front position in time obtained by Kitagawa et al.[22] (+) and the numerical simulation (——).

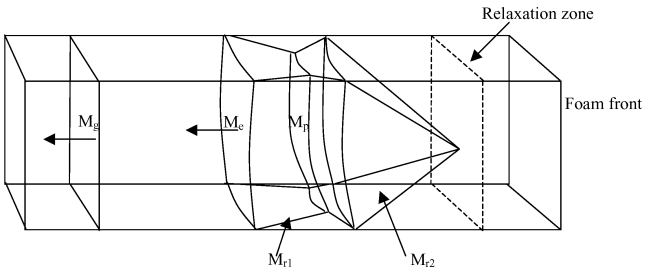

Fig. 5 Proposed solid-phase shock-wave diagram for the three-dimensional shock-wave interaction with a deformable foam.

The experimental data presented by Kitagawa et al.[22] were obtained using a holographic interferometery and therefore present a three-dimensional picture of the interaction. In Fig. 5, a three-dimensional waves' configuration diagram is proposed for the head-on interaction of the shock wave with polyurethane foam in a rectangular shock tube. Because of the rectangular shape of the shock tube and the friction force acting on the polyurethane foam by the shock-tube sidewalls, three-dimensional waves' interactions were developed at the shock-tube sidewalls corners. These interactions influence farther upstream on the shock-wave configuration. The shock wave moving from right to left in the gaseous phase (marked as M_g in Fig. 5) induces a nonuniform interactions (caused by sidewall friction) with the solid phase, which results in a relatively weak positive solid-phase velocity field. The elastic wave (marked as M_e in Fig. 5) appears behind the transmitted shock wave; M_e will therefore be a nonplanar wave. The reflected waves from the interaction between the elastic wave M_e and the shock-tube sidewalls (marked as M_{r1} in Fig. 5) formed a rectangular pyramid, caused by the rectangular shape of the shock tube. When the reflected waves M_{r1} interact with the precursor of the plastic wave (marked as M_p in Fig. 5), more reflections occur and are propagating to the shock-tube sidewalls, which then perform more reflections and multiple interactions' configuration moving upstream. Because of the elastic movement of the foam, a relaxation zone will be formed between the elastic-plastic zone and the foam front. The relaxation zone can also be seen in Fig. 3 (marked as area 2). The predictions of the density field obtained for 1 ms after the shock impact on the foam is presented in Fig. 5. From the proposed three-dimensional waves' configuration diagram it can be seen that the typical λ shape of the foam is formed as a result of the interactions between the reflected waves M_{r1} and the precursor of the plastic wave M_p.

The predictions of the two-dimensional simulations for this interaction are presented in Figs. 6 and 7. As can be seen, the numerical simulation qualitatively predicts the typical λ shape deformation of the foam, marked as area 1 in Figs. 3 and 6. Similarly, the area of minimum density values, marked as area 2 in Figs. 3 and 6, can be observed. Although Kitagawa et al.'s experimental data[22] demonstrated three-dimensional behavior, our predicted two-dimensional flowfield demonstrated fairly well the projection of the three-dimensional typical λ shape structure in the symmetrical two-dimensional plane and therefore validates our proposed three-dimensional waves' configuration diagram shown in Fig. 5. In addition, conducting the same simulations without solid wall-friction model did not yield the typical λ shape structure in the solid phase. Therefore, based on the observations just mentioned it can be concluded that the origin of the typical λ shape deformation in the solid phase is the existence of solid wall friction, whereas the wall friction for the gaseous phase was assumed to be small and therefore neglected.

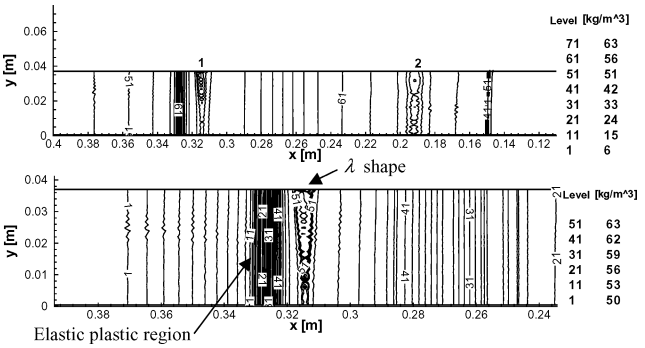

Fig. 6 Predicted solid density contours (top figure) and a magnification of the λ shape region (marked as zone 1 in the top figure) for the unsteady interaction between a planar shock wave and polyurethane foam.

Solid-phase pressure field and y and x stress components as predicted for the conditions just mentioned are presented in Figs. 7a, 7b, and 7c, respectively. It is clear that the solid flowfield could be divided generally into four areas: 1) gas-induced flow area, which is relatively not affected by three-dimensional effects, and the gas flow is induced by the transmitted shock wave that propagates in the gas phase and it impacts on the solid-phase behavior; 2) high compression area, which is characterized by a compression wave and an elastic-plastic front area; 3) a relaxation area, which is characterized by a minimum density and stress (Fig. 5); and 4) foam front area, where the gas is penetrating into the foam. The density minima in the solid phase causes a pressure and density minima in the gas flowfield as well, because of the growth of local porosity. The obtained results are similar to the one-dimensional investigation of Levi-Hevroni.[10] The foam front moves faster then the gas density minima area. Therefore, the gas that was initially inside the foam emerges out from the foam front, and a contact surface can be observed.[18,19] While taking the wall-friction effect into consideration, the influence of the shock-tube geometry can also be noticed in the two-dimensional numerical simulations. Although only two-dimensional numerical simulations were conducted, a three-dimensional waves' diagram for this interaction is proposed and presented in Fig. 5. As can be seen, the predictions of the two-dimensional numerical simulations demonstrate the validity of the proposed model. The waves' interaction and their two-dimensional effects can be notable in Figs. 6 and 7 (i.e., solid-phase density, pressure, and stresses field). However, it was found out that examining the shear wave's configuration, via a vorticity flowfield, will simplify the explanations for the multidimensional effects. Figure 7d presents the solid-phase vorticity field, defined by

$$\omega = \nabla \times \boldsymbol{u} \tag{28}$$

Two major shear bands are clearly seen in Fig. 7d. The first is created as a result of the gas flow behind the transmitted shock wave moving in the gas phase. The gas flows behind this shock-wave transfer momentum to the solid phase. As a result, the foam starts to move. Because of the foam movement and its interaction with the shock-tube sidewall, a shear band in the solid phase is formed. This shear band interacts with the elastic-plastic front and reflects toward the shock tube sidewall. The second shear wave is generated by the

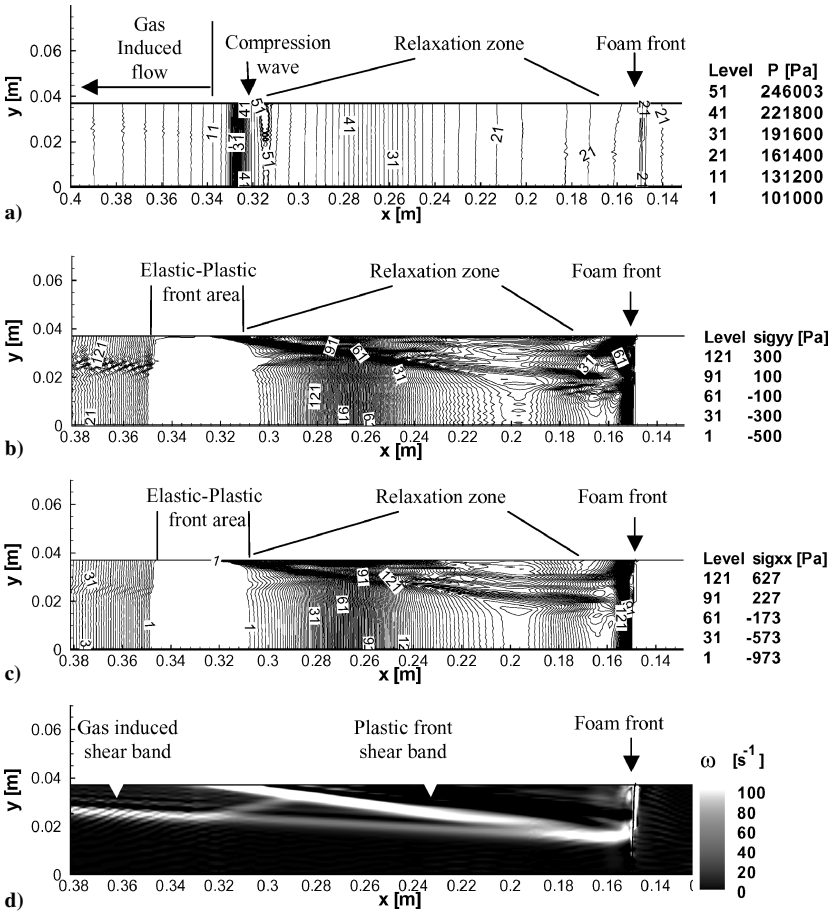

Fig. 7 Numerical prediction of a) solid pressure, b) *y*-direction stress component, c) *x*-direction stress component, and d) vorticity contours.

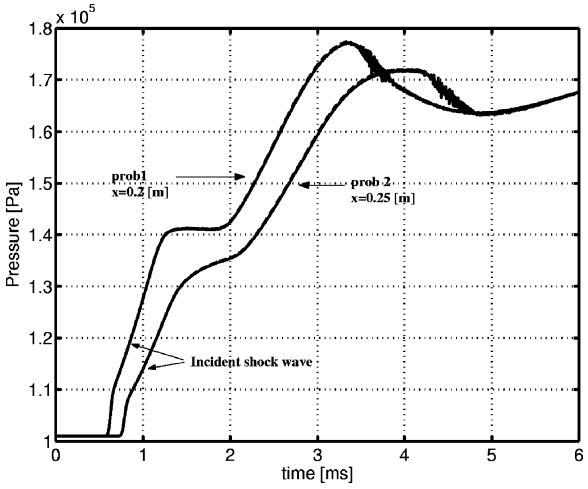

Fig. 8 Gas pressure trajectories on the shock-tube sidewall vs time at $X = 0.2$ and 0.25 m from the foam interface initial position, with and without wall-friction model (—— and – – –, respectively).

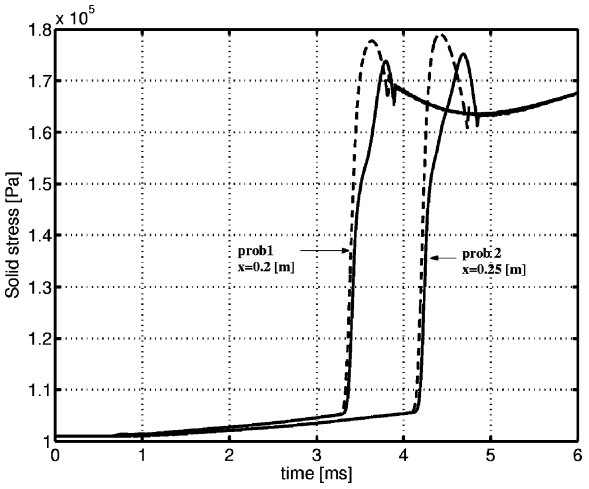

Fig. 9 Predicted foam stress trajectories on the shock-tube sidewall vs time at $X = 0.2$ and 0.25 m from the foam interface initial position, with and without wall-friction model (—— and – – –, respectively).

elastic plastic front and propagates back to the foam front. These major shear bands interact with the elastic-plastic region and create a local disturbance in the flowfield near to the plastic zone, which finally distorts the foam in the typical λ shape as photographed by Kitagawa et al.,[22] presented in the proposed wave diagram model (shown in Fig. 5) and predicted by the present two-dimensional numerical simulation.

The predictions of the numerical simulations for the gas pressure and the foam stress (defined as the second invariant of the complete stress tensor, i.e., the stress tensor plus the hydrostatic pressure) on the shock-tube sidewall are presented in Figs. 8 and 9, respectively. In these figures, the solid and the dashed lines present the predictions of the numerical simulations with solid-phase wall-friction model and with free-slip boundary condition, respectively. In each figure, two traces (referred as prob1 and prob2) of the gas pressure and the foam stress traces are presented. The locations of theses probes are on the shock-tube sidewall, 0.2 and 0.25 m from the initial foam interface position. As can be seen, the influence of the solid-phase wall-friction model on the measurements of the gas-phase pressure is negligible. Two distinct compression periods are presented. The first results from the incident shock wave moving in the gas, and the second (starting at 1.9 ms) results from the pores densification because of the solid movement. As for the solid stress, the stress wave arrives to prob1 after 3.2 ms, and it is identical for both cases,

that is, calculations with and without wall-friction model. However, as can be seen different slopes (resulting from the expanded elastic-plastic front with the wall-friction model, i.e., the λ shape) and peaks are obtained. The difference in the wave shape is clearly shown. It is also noted that in the lack of solid wall friction, the densification front velocity is faster.

Because of the large deformation of the foam, its front passes prob1 and prob2 after 3.8 and 4.75 ms (see Fig. 4). These passes are noticeable by the probes (see Figs. 8 and 9) by short periods of oscillation, and then both the gas pressure and the solid stress traces have the same values.

V. Conclusions

A two-dimensional two-phase numerical study was performed to simulate the unsteady head-on collision of planar shock-wave interaction with deformable open cell foam. A simple general physical model was proposed for the three-dimensional waves' configuration in the solid phase, that is, the deformable foam. The numerical predictions were validated with experimental results of Skews et al.[19] for the one-dimensional case, and Kitagawa et al.[22] for the two- and three-dimensional effects of the waves' configuration of the solid phase. Good agreements were evident in both cases. The predictions of the numerical simulation demonstrated the influence of the solid wall-friction model on the history of the foam stress at the shock-tube sidewall. It was obtained that its influence on the gas pressure histories is negligible.

From the predictions of the numerical simulations, it appears that the flow-field of the foam could be divided into four zones, namely, gas-induced flow, elastic-plastic front area, relaxation area, and the foam front area. The dimensional effect was presented, characterized by a regular refection from the shock-tube sidewalls.

Based on the numerical simulation and its good comparison with Kitagawa et al.'s three-dimensional experimental data,[22] it was concluded that our proposed three-dimensional waves' configuration diagram is valid and that the origin of the typical λ shape deformation is the existence of solid wall friction. To describe the flowfield correctly, a three-dimensional numerical model is required because the results obtained by Kitagawa et al.[22] are strongly affected by three-dimensional shock interactions.

References

[1]Baer, M. R., "A Numerical Study of Shock Wave Reflections on Low Density Foam," *Shock Waves*, Vol. 2, No. 2, 1992, pp. 121–124.

[2]Bear, J., Sorek, S., Ben-Dor, G., and Mazor, G., "Displacement Waves in Saturated Thermoelastic Porous Media. I. Basic Equations," *Fluid Dynamics Research*, Vol. 9, No. 1–3, 1992, pp. 155–164.

[3]Levy, A., Sorek, S., Ben-Dor, G., and Bear, J., "Evolution of the Balance Equations in Saturated Thermoelastic Porous Media Following Abrupt Simultaneous Changes in Pressure and Temperature," *Transport in Porous Media*, Vol. 21, No. 3, 1995, pp. 241–268.

[4]Levy, A., Sorek, S., Ben-Dor, G., and Skews, B., "Wave Propagation in Saturated Rigid Porous Media: Analytical Model and Comparison with Experimental Results," *Fluid Dynamics Research*, Vol. 17, No. 2, 1996, pp. 49–65.

[5]Levy, A., Ben-Dor, G., and Sorek, S., "Numerical Investigation of the Propagation of Shock Waves in Rigid Porous Materials: Development of the Computer Code and Comparison with Experimental Results," *Journal of Fluid Mechanics*, Vol. 324, 1996, pp. 163–179.

[6]Skews, B. W., Levy, A., and Levi-Hevroni, D., "Shock Wave Propagation in Porous Media," *Handbook on Shock Waves*, edited by G. Ben-Dor, O. Igra, and T. Elperin, Academic Press, Boston, 2000, Chap. 15.1.

[7]Bear, J., and Bachmat, Y., *Introduction to Modeling of Transport Phenomena in Porous Media*, Kluwer Academic, Dordrecht, The Netherlands, 1990.

[8]Sorek, S., Bear, J., Ben-Dor, G., and Mazor, G., "Shock Waves in Saturated Thermoelastic Porous Media," *Transport in Porous Media*, Vol. 9, No. 1–2, 1992, pp. 3–13.

[9]Levy, A., "Wave Propagation in a Saturated Porous Medium," Ph.D. Dissertation, Dept. of Mechanical Engineering, Ben-Gurion Univ. of the Negev, Beer Sheva, Israel, June 1995.

[10]Levi-Hevroni, D., "Non-Linear Waves Propagation in Multiphase Porous Media," Ph.D. Dissertation, Dept. of Mechanical Engineering, Ben-Gurion Univ. of the Negev, Beer Sheva, Israel, May 2000.

[11]Mazor, G., Ben-Dor, G., Igra, O., and Sorek, S., "Shock Wave Interaction with Cellular Materials. Part I: Analytical Investigation and Governing Equations," *Shock Waves*, Vol. 3, No. 3, 1994, pp. 159–165.

[12]Gelfand, B. E., Gubanov, A. V., and Timofeev, E. I., "Interaction of Shock Waves in Air with a Porous Barrier," *Izvestiia Akademii Nauk SSSR. Mekhanika Zhidkosti i Gaza*, Vol. 4, 1983, pp. 79–84.

[13]Gvozdeva, L. G., and Faresov, Y. M., "Calculating the Parameters of Steady Shock Waves in Porous Compressible Media," *Soviet Physics—Technical Physics, Zh. Tekh. Fiz.*, Vol. 55, 1985, pp. 773–775.

[14]Baer, M. R., "Numerical Studies of Dynamic Compaction of Inert and Energetic Granular Materials," *Journal of Applied Mechanics*, Vol. 55, 1988, pp. 36–43.

[15]Powers, J. M., Stewart, D. S., and Krier, H., "Analysis of Steady Compaction Waves in Porous Materials," *Journal of Applied Mechanics*, Vol. 56, 1989, pp. 15–24.

[16]Bear, J., and Sorek, S., "Evolution of Governing Mass and Momentum Balances Following an Abrupt Pressure Impact in Porous Medium," *Transport in Porous Media*, Vol. 5, 1990, pp. 169–185.

[17]Levy, A., Ben-Dor, G., Skews, B. W., and Sorek, S., "Head-On Collision of Normal Shock Waves with Rigid Porous Materials," *Experiments in Fluids*, Vol. 15, 1993, pp. 183–190.

[18]Levi-Hevroni, D., Levy, A., Ben-Dor, G., and Sorek, S., "Numerical Investigation of the Propagation of Planar Shock Waves in Saturated Flexible Porous Materials: Development of the Computer Code and Comparison with Experimental Results," *Journal of Fluid Mechanics*, Vol. 462, 2002, pp. 285–306.

[19]Skews, B. W., Atkins, M. D., and Seitz, M. W., "Shock Wave Interactions with Porous Compressible Materials," *Journal of Fluid Mechanics*, Vol. 253, 1993, pp. 245–265.

[20]Kitagawa, K., Jyonouchi, T., and Yashura, M., "Drag Difference Between Steady and Shocked Gas Flows Passing Through a Porous Body," *Shock Waves*, Vol. 11, No. 2, 2001, pp. 133–139.

[21]Levy, A., Levi-Hevroni, D., Sorek, S., and Ben-Dor, G., "Derivation of Forchheimer Terms and Their Verification by Application to Compaction Waves Propagation in Porous Media," *International Journal of Multiphase Flow*, Vol. 25, No. 3, 1999, pp. 683–704.

[22]Kitagawa, K., Kainuma, M., Ojima, H., Lomatsu, M., Takayama, K., and Yashura, M., "Visualization of Shock Wave/Foam Interaction," 23rd ISSW, Fort Worth, TX, 2001.

[23]Li, H., Levy, A., and Ben-Dor, G., "Analytical Prediction of Regular Reflection over Rigid Porous Surfaces in Pseudo-Steady Flow," *Journal of Fluid Mechanics*, Vol. 282, 1995, pp. 219–232.

[24]Skews, B. W., "Oblique Reflection of Shock Waves from Rigid Porous Material," 10th Mach Reflection Symposium, Denver, CO, 1992.

[25]Kobayashi, S., Adachi, T., and Suzuku, T., "Regular Reflection of a Shock Wave over a Porous Layer: Theory and Experiment," *Shock Waves @ Marseille IV*, edited by R. Brun and L. Z. Dumitrescu, Springer, Berlin, 1995, pp. 175–180.

[26]Malamud, G., Levi-Hevroni, D., and Levy, A., "Two-Dimensional Model for Simulating the Shock Wave Interaction with Rigid Porous Materials," *AIAA Journal*, Vol. 41, No. 4, 2003, pp. 663–673.

[27]Skews, B. W., "Oblique Reflection of Shock Waves from Rigid Porous Materials," *Shock Waves*, Vol. 4, No. 3, 1994, pp. 145–154.

[28]Wilkins, M. L., "Calculations of Elastic Plastic Flow," *Methods in Computational Physics III*, Academic Press, New York, 1964, pp. 211–247.

[29]Terzaghi, K., *Erbaumechnik auf Bodenphysikalisch Grundlag*, Franz Deuticke, Leipzig, Germany, 1925.

[30]Levy, A., Ben-Dor, G., and Sorek, S., "Numerical Investigation of the Propagation of Shock Waves in Rigid Porous Materials—Flow Field Behavior and Parametric Study," *Shock Waves*, Vol. 8, No. 3, 1998, pp. 127–137.

[31]Zaretsky, E., and Ben-Dor, G., "Thermodynamic Law of Corresponding Shock States in Flexible Polymeric Foams," *Journal of Engineering Materials and Technology*, Vol. 118, Oct. 1996, pp. 493–502.

[32]Gibson, L. J., and Ashby, M. F., *Cellular Solids—Structure and Properties*, Program Press, Hill Hall, Oxford, 1988.

C. Kaplan
Associate Editor